Construction and Building Materials 145 (2017) 157–165

Contents lists available at ScienceDirect

Construction and Building Materials

journal homepage: www.elsevier.com/locate/conbuildmat

Pore structure description of mortars containing ground granulated blast-furnace slag by mercury intrusion porosimetry and dynamic vapour sorption

Natalia Alderete [a,b], Yury Villagrán [a,b], Arn Mignon [a], Didier Snoeck [a], Nele De Belie [a,*]

[a] Magnel Laboratory for Concrete Research, Department of Structural Engineering, Faculty of Engineering and Architecture, Ghent University, Tech Lane Ghent Science Park, Campus A, Technologiepark Zwijnaarde 904, B-9052 Ghent, Belgium
[b] LEMIT, CONICET, 52 entre 121 y 122 s/n, 1900 La Plata, Argentina

HIGHLIGHTS

- DVS and MIP tests are sensitive to pore size distribution changes over time.
- Differences in DVS and MIP results are expected given their different approaches.
- Consideration of the techniques limitations leads to a comprehensive analysis.
- Restrictive pore sizes greatly influence the accessibility into the matrix.
- Pore connectivity has more influence on the test results than pore volume.

ARTICLE INFO

Article history:
Received 25 May 2016
Received in revised form 28 March 2017
Accepted 31 March 2017

Keywords:
Supplementary cementitious materials
Mercury intrusion porosimetry
Dynamic vapour sorption
Ground granulated blast-furnace slag
Porosity
Pore connectivity

ABSTRACT

The description of the pore structure is a key aspect when studying the durability of cement-based materials. Many techniques have been developed over the years in order to describe the actual complex microstructure of these materials. These techniques can be useful to determine the change in pore structure when supplementary cementitious materials are used and also track its evolution with time. This paper particularly aims to describe the changes in the pore structure of mortars with contents of 20, 40 and 60% of ground-granulated blast-furnace slag (GGBFS) in replacement of cement, at the ages of 28 and 90 days. Two widely accepted techniques were applied: dynamic water vapour sorption (DVS) and mercury intrusion porosimetry (MIP). For the data analysis from the DVS test, the Barret-Joyner-Halenda (BJH) model was used for pore size distribution assessment. Moreover, since the extent of this model does not cover the smallest range of pores, calculations with the Dubinin-Radushkevich (DR) model were also made. Results from the MIP test were used to characterize the threshold diameter, the smallest intrudable diameter, and the intrudable porosity. GGBFS replacement leads to a slight increase in porosity values at 28 days, especially seen in the DVS results for the pore size range of 0.002–0.05 μm. DVS results at 90 days for the mix with 40% slag replacement showed a marked reduction in porosity and a shift in pore structure to the finer pore size range when compared to the 28 day results. For all cases, the total porosity was found to be less influential on the test results than pore connectivity.

1. Introduction

Description of the pore structure immediately outlines several other properties, since the pore structure has a great influence on the physical, mechanical and durability behaviours. When supplementary cementitious materials (SCMs) are used, changes in pore structure normally occur over time and in relation to the reaction degree of the SCM, with consequential modifications of the above-mentioned properties. Particularly, the use of ground granulated blast-furnace slag (GGBFS) generally implies an improvement in durability-related properties [1–3]. GGBFS shows both a cementitious nature and pozzolanic activity, i.e. a reaction in the presence of lime [4]. The combination of these effects normally leads to a pore volume reduction with time [1,2,5–7]. In addition, given that GGBFS is a by-product of the steel industry,

* Corresponding author.
E-mail addresses: nataliamariel.alderete@ugent.be (N. Alderete), yuryvillagran@conicet.gov.ar (Y. Villagrán), arn.mignon@ugent.be (A. Mignon), didier.snoeck@ugent.be (D. Snoeck), nele.debelie@ugent.be (N. De Belie).

http://dx.doi.org/10.1016/j.conbuildmat.2017.03.245
0950-0618/

its use also helps to reduce clinker production (one of the major sources of CO_2 emissions), which provides an added value to this by-product.

Much effort has been invested in accurately describing the pore structure of cementitious materials [8–13], however, no model or method has been universally acknowledged for providing a complete description and characterization. Nevertheless, limitations do not impede that important information can be obtained from the different current experimental techniques, which may be used as input for analytical models. In this sense, it is important not to forget the critical assumptions made for each method, and to keep a reasonable perspective of the obtained results for their application.

The dynamic vapour sorption (DVS) test provides information regarding pore structure through an experimental set-up to measure the equilibrium between the mass water content of the sample and the relative humidity (RH), at a constant temperature. Several authors [8,12–14] have pointed out some benefits of the use of water sorption instead of other gases for sorption techniques. One of those advantages is that water molecules are relatively smaller than CO_2 or N_2 [8], which allows them to penetrate not only the small sized pores but also into the so-called ink bottle pores. Moreover, it is not necessary to degas the sample prior to the measurements, hence avoiding possible microstructural damage. Furthermore, the test can be performed at room temperature, which is of course quite convenient since there is no need for a major temperature-conditioning equipment. Nonetheless, there are some limitations in the theories of adsorption which mathematically describe the results. For instance, the monolayer is a fictional quantity and not a physical reality as the BET theory implies that the surface is never completely covered until the saturated vapour pressure is reached [15]. Furthermore, calculations of the pore size distribution also have theoretical assumptions, such as the consideration of cylindrical pore shapes [16]. In spite of these limitations, quantitative information can be obtained from the isotherms, which is then used to calculate specific surface area and pore size distribution.

The mercury intrusion porosimetry (MIP) test has been widely used to analyse the microstructure of cementitious materials [13,17–20]. Nevertheless, its interpretation also requires some assumptions and theoretical simplifications, such as the same accessibility to the external surface of all the pores, cylindrical-shaped pores, and absence of ink-bottle pores, all of which vary from the actual pore structures of cementitious materials. Diamond [21] has described these -and other-drawbacks fairly well, but nevertheless still accepted the use of the threshold diameter (d_{th}) and intrudable pore volume (ϕ_{in}) as indexes of the pore structure for qualitative comparison. In fact, from experimental results, three main features have been described to be the most-representative and most-useful for modelling [22]: the intrudable porosity (ϕ_{in}), the smallest intrudable pore diameter (d_{min}), and the threshold pore diameter (d_{th}). It has been clearly stated that ϕ_{in} should not be associated with the total porosity [21–23], but rather with the accessible porosity, as it is equivalent to the volume of mercury intruded corresponding to the highest point in each cumulative curve. On the other hand, the precise determination of d_{th} is controversial. Aligizaki [23] described it as the diameter above which there is comparatively little mercury intrusion, and immediately below which starts a vast intrusion of mercury. In order to objectively assess the value of d_{th}, several authors [22,24,25] have established some methods to provide comparable results. Those methods are described, used, and discussed later in this paper to compare the different obtained values.

In order to convey a comprehensive description of pore structure, mortars with 20, 40 and 60% w/w of GGBFS as replacement of Portland cement were tested at different ages using the DVS and the MIP tests. This paper discusses the data obtained considering the theoretical assumptions of each technique, and describes the pore structure of mortars in the presence of GGBFS and its evolution over time.

2. Materials and methods

In order to perform the tests, three mortar mixes were designed with a water/binder (w/b) ratio of 0.45 and a sand/binder (s/b) ratio of 3. The mixes were designated as S20, S40 and S60, having respectively 20, 40 and 60% w/w of GGBFS with respect to total binder content. The mixing procedure and the compressive strength test were performed in accordance with EN 196-1 [26]. Mortar samples were cured in a humid chamber at 20 ± 2 °C and 95 ± 5% RH for 28 and 90 days, and then conditioned for testing. Water absorption (WA), apparent density, open porosity, and resistivity in the saturated state were determined at 90 days. Compressive strength was measured at 28 days.

For the determination of the apparent density and open porosity, samples were first submitted to a vacuum for two hours and then water was drawn into the vacuum chamber until the sample became fully immersed. After 24 h the sample was removed and weighed, which was denoted as saturated mass in air (m_{sa}). The samples were also weighed in water, and denoted as saturated mass in water (m_{sw}). Then, samples were subjected to drying in an oven at 50 °C until the change in mass was lower than 0.1% in a 24 h period, and denoted as dry mass (m_d). The apparent density was calculated as the ratio between m_d and ($m_{sw} - m_d$), multiplied by the density of water. The open porosity was calculated as ($m_{sa} - m_d$)/($m_{sa} - m_{sw}$). In this paper, total porosity of concrete was linked to the water-permeable or open porosity. This is in fact a simplification (in reality, pores that are not connected to the exterior are not considered in the water-permeable porosity), but this accessible porosity is the responsible for transport mechanisms. Table 1 shows the results of the mentioned tests.

Ordinary Portland cement (OPC) type CEM I 52.5, normalized siliceous sand (0/2) and tap water were used in all mixes. The chemical compositions of the OPC and the GGBFS are shown in Table 2. The particle size distributions of the OPC and GGBFS (Table 3) were determined by means of laser diffractometry using a Malvern Mastersizer 2000 E particle analyser with wet unit Hydro 2000SM. Values of refraction index (n) and absorption coefficient (k) shown in Table 3 were selected according to the values found in literature [27,28] and tested to select the ones which had the best fit and lowest weighed residual to the obtained data.

2.1. Mercury intrusion porosimetry (MIP) test

MIP tests were performed on samples of approximately 1.5 cm^3. A Pascal 440 mercury porosimeter with a maximum load capacity of 420 MPa was used. However, the maximum pressure was limited to 200 MPa in order to avoid cracks induced by the mercury pressure [29]. The adopted mercury surface tension and contact angle between the mercury and the solid surface were 482 mN/m and 142°, respectively. A blank run for differential mercury compression was made to correct the volume measurements [18]. The pore diameters related to the pressure applied were calculated with the Washburn equation [30].

To minimize microstructural damage during pre-conditioning, samples were first dried at 40 °C for 24 h, and then vacuum-dried at 20 ± 2 °C for two weeks at 0.1 bar. This preconditioning technique has been validated through microstructural analyses in previous studies [14,31].

The data obtained from the MIP test was used to determine d_{min}, ϕ_{in}, and d_{th}. The calculation of d_{th} was made considering two methods:

i) the 5% method: this method was used by [24], where d_{th} is calculated as the point in which the porosity is 5% of ϕ_{in}. This offers the advantage of a conventional value and protocol, since there is no need to assume at which point sufficient mercury has penetrated into the porous system. The d_{th} obtained by using this method has been denoted as d_{th} (5%).
ii) the tangent method: this method was first adopted by Liu and Winslow [25] to determine the threshold diameter as that corresponding to the intersection of tangent lines on the cumulative distribution curve at the smallest diameter that did not exhibit significant intrusion and the largest diameter that did. Using this approach as a basis, Ma [22] fitted points at

Table 1
Properties of mortars (mean ± standard deviation).

Mixes	S20	S40	S60
Compressive strength (MPa)[28 d]	75.0 ± 1.2	56.0 ± 1.6	49.0 ± 1.6
Compressive strength (MPa)[90 d]	75.4 ± 0.9	61.2 ± 1.7	54.1 ± 1.6
Water absorption (%)[90 d]	5.9 ± 0.4	6.7 ± 0.2	7.0 ± 0.2
Apparent density (g/cm^3)[90 d]	2.50 ± 0.02	2.55 ± 0.01	2.55 ± 0.04
Porosity (%)[90 d]	12.8 ± 0.8	14.5 ± 0.4	15.1 ± 0.5
Saturated resistivity (kohm·cm) [90 d]	20.64 ± 1.2	23.08 ± 0.8	29.68 ± 2.3

Table 2
Chemical properties of OPC and GGBFS.

XRF chemical analysis (%)							
CEM I				GGBFS			
CaO	64.67	MgO	0.95	CaO	36.16	Na_2O	1.91
SiO_2	20.74	K_2O	0.77	SiO_2	28.89	Fe_2O_3	0.95
Al_2O_3	4.91	Na_2O	0.27	MgO	12.14	TiO_3	0.46
SO_3	2.96	Cl	0.07	Al_2O_3	8.62	K_2O	0.43
Fe_2O_3	1.52			Na_2O	1.91	MnO	0.43

Table 3
Particle size distribution and optical parameters of OPC and GGBFS.

	Particle size distribution (μm)			Optical parameters	
Material	dv10	dv50	dv90	n	k
GGBFS	1.15	12.94	67.57	1.60	0.100
OPC	4.88	20.14	58.53	1.73	0.003

which diameters are obviously below d_{th} and above d_{th}, to determine two tangent lines. In this study, the range of the points to be fitted is determined analysing the second derivative in the differential curve. Furthermore, according to the cumulative curve shape obtained, it is possible to use the tangent method to identify two different d_{th}: a primary d_{th} denoted as d_{th1}(TG), which represents the first percolation process; and a secondary d_{th} denoted as d_{th2}(TG),which represents the virtual size after the second percolation process has been reached. This secondary threshold diameter provides information about the presence of choke points.

2.2. Dynamic water vapour sorption (DVS) test

For the DVS tests, samples were taken out of the humid chamber at 20 ± 2 °C and 95 ± 5% RH at the age of 28 and 90 days, and ground and sieved between 500 and 1000 μm. This particle size for the sample was considered as a good compromise between test duration and practicality [14]. Carbonation was prevented by storing samples in sealed containers in the presence of soda lime, immediately after being ground and until the time of testing (0.5–3 h). The device was set at 20 °C, and a dm/dt < 0.002 wt.%/min was set as a detection limit to continue to the following RH level. The RH levels at which samples were subsequently equilibrated included 98–90–80–70–60–50–40–30–20–10–5–0% RH. Since samples were taken out of the humid chamber and readily tested, they were first equilibrated to 98% RH and then to a complete desorption-sorption cycle.

Porosity was classified, according to [32], into micropores (<0.002 μm), mesopores (0.002–0.05 μm) and macropores (>0.05 μm). The Barret, Joyner and Halenda (BJH) method [16] was used for the calculation of the pore size distribution in the mesopore range. This method, based on the Kelvin model, considers that capillary and adsorbed water phases exist in cylindrical pores and calculations of the pore size distribution are made by iterative step-by-step calculations [8]. The Dubinin-Radushkevich (DR) equation [33] was used to calculate the pore size distribution in the micropore range. The method is based on the assumptions of a change in potential energy between the gas and adsorbed phases.

3. Results

3.1. MIP tests

Figs. 1–3 show the cumulative intruded volume curve of S20, S40 and S60, respectively, at 28 (a) and 90 (b) days. The three fitting lines used for the calculation of d_{th} (TG) can also be seen with their respective fitting equations. The point of intersection of those lines is the graphical representation of d_{th}(TG). According to the curve shape, a primary d_{th1}(TG) and a secondary d_{th2}(TG) could be determined for S20 and S60, but a primary d_{th}(TG) for S40 seems not so evident. In any case, d_{th1}(TG) and d_{th2}(TG) were determined for comparative purposes. The highest point in the curve corresponds to ϕ_{in} and the diameter reached at that point is (d_{min}. Figs. 1–3 also display the threshold diameter obtained with the 5% method, d_{th}(5%), which is the point corresponding to 5% of ϕ_{in}. The same graphical and analytical approach was used for all mixes.

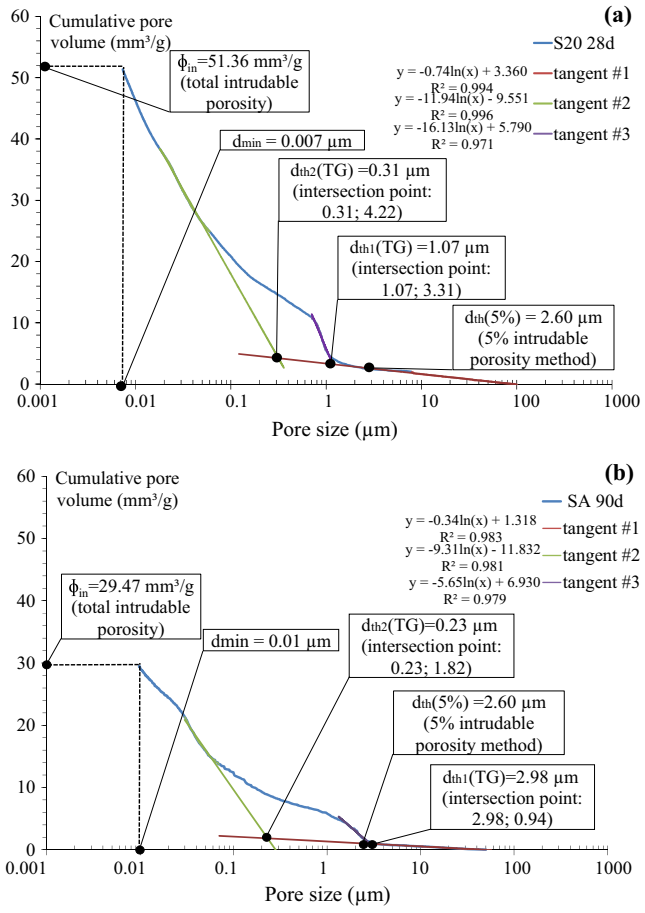

Fig. 1. Cumulative intruded volume of S20 with the corresponding d_{th1}(TG); d_{th2}(TG); d_{th}(5%), d_{min}, and ϕ_{in}, at 28 (a) and 90 (b) days.

Considering also the classification of pores as described in [32], values of the volume of pores in the macropores and mesopores range were calculated from the cumulative intruded curve data. Fig. 4 shows the values of those ranges for all mixes at 28 and 90 days.

3.2. DVS tests

Desorption-sorption isotherms of S20, S40 and S60 are shown in Fig. 5 at 28 (a) and 90 (b) days, respectively. All sorption curves

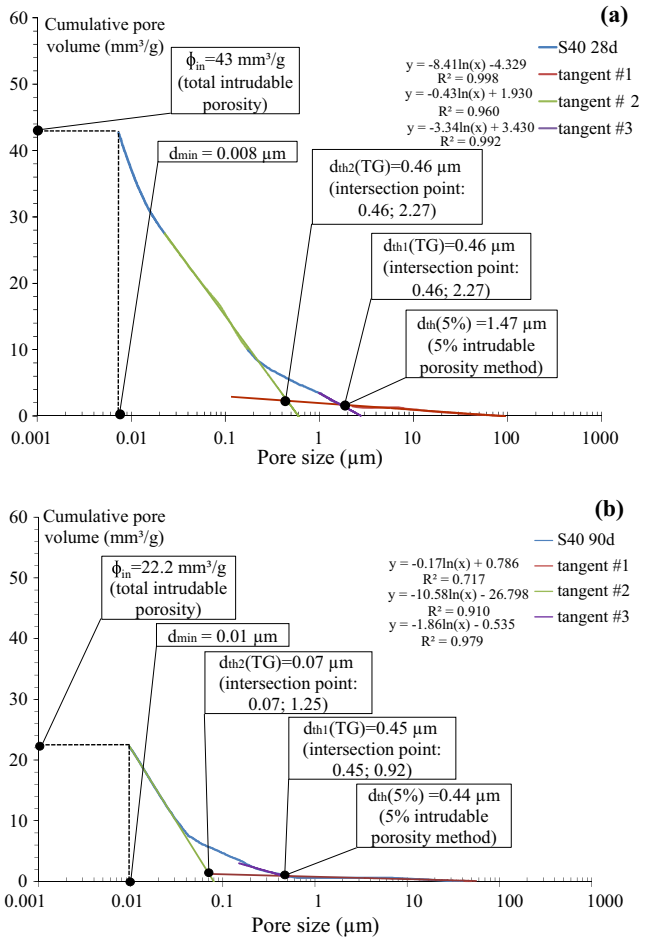

Fig. 2. Cumulative intruded volume of S40 with the corresponding $d_{th1}(TG)$; $d_{th2}(TG)$; $d_{th}(5\%)$, d_{min} and ϕ_{in}, at 28 (a) and 90 (b) days.

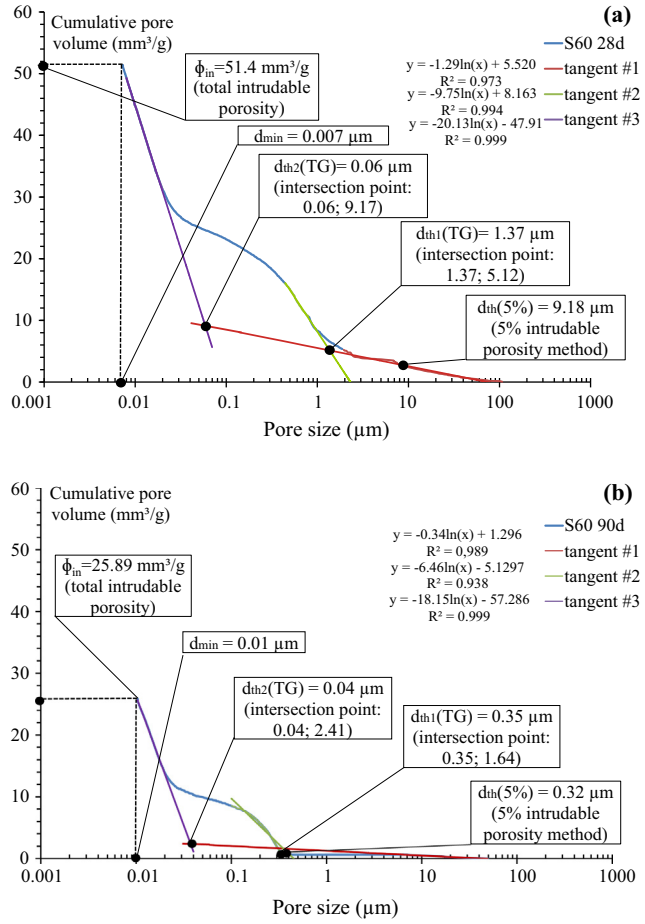

Fig. 3. Cumulative intruded volume of S60 with the corresponding $d_{th1}(TG)$; $d_{th2}(TG)$; $d_{th}(5\%)$, d_{min} and ϕ_{in}, at 28 (a) and 90 (b) days.

exhibit a Type IV isotherm shape [34], and a marked hysteresis can be seen for all samples and RH values. The desorption branch shows an abrupt decrease after 40% RH in every case, whereas in the case of the sorption curve, there is a steep rise above 60% RH, showing that a cementitious matrix is mainly composed of mesopores. At 28 days, the slope in the adsorption branch increases as the slag replacement increases, but there are no significant differences for RH < 30%.

Fig. 6 shows the derivative (a) and cumulative (b) pore size distribution of the three mixes at 28 days, and the derivative (c) and cumulative (d) pore size distribution at 90 days calculated with the BJH method, and the MIP data. In the case of the latter, the smallest pore sizes were registered only between 0.007 and 0.01 µm with the pressure level applied.

Results from the BJH and DR calculations for the pore volume of mesopores and micropores, respectively, are shown in Fig. 7 for all mixes at 28 and 90 days.

Fig. 8 (a) shows the results of porosity obtained from WA, MIP and DVS. It should be noted that the porosity does not give any information concerning pore size distribution or pore connectivity. The interest of WA porosity is limited to the determination of the extent to which slag replacement increases the amount of permeable pores. Both WA porosity and MIP measure the pore volume through absorption/intrusion of fluids. Then, a different measuring mechanism results in different values from those obtained by DVS. Since the main effect of the slag is seen in the shift towards smaller pores (between 0.002 and 0.05 µm), the largest pores (main

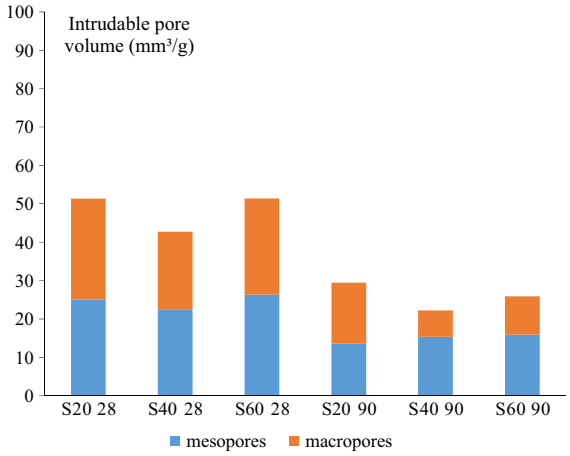

Fig. 4. Pore volume of mesopores and macropores for all mixes at 28 and 90 days, obtained from MIP data.

contributors to the total pore volume) are not significantly affected by this refinement action.

Fig. 8 (b) shows the variation with time of the ratio between MIP and DVS results in relation to pore volume, for all mixes at 28 and 90 days. For comparison purposes, the pore volume for the sizes that both methods are able to measure in the mesopore range (0.007–0.05 µm) was considered. Since in the case of the MIP test, only sizes down to 0.007 µm were registered with the

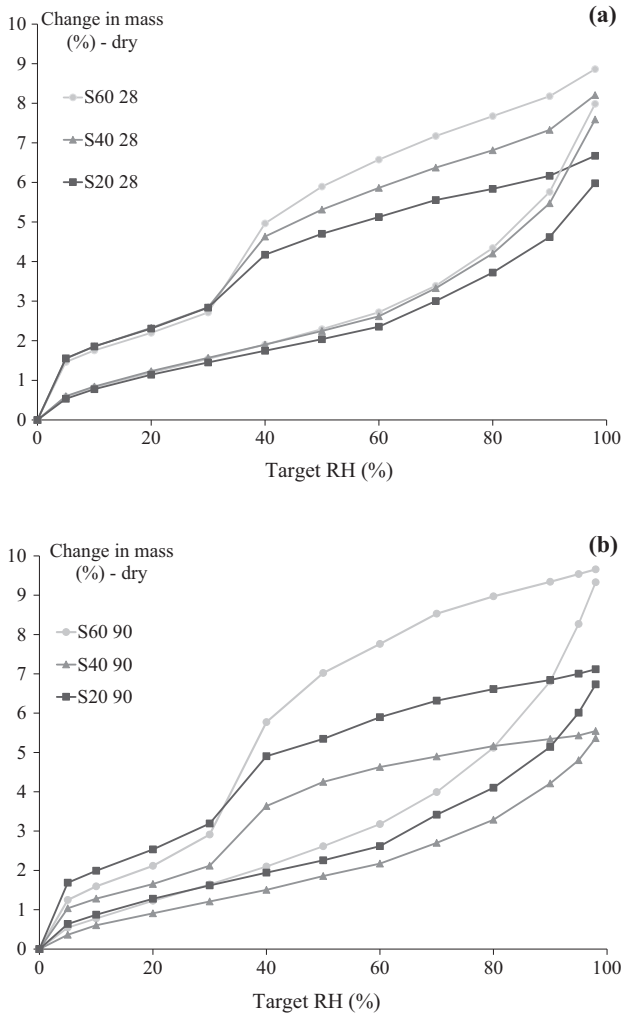

Fig. 5. Sorption isotherms of S20, S40 and S60 at 28 (a) and 90 (b) days.

pressure level applied, also only the pores between 0.007 and 0.05 μm were computed from the DVS data. Each point represents the percentage of the volume of mesopores obtained from MIP in relation to the volume of mesopores obtained from DVS with the BJH calculation for all mixes at 28 and 90 days. The values between brackets at each point, (a, b), represent the volume of mesopores assessed by the MIP test (a), and the volume of mesopores assessed by the DVS test (b).

4. Discussion

4.1. MIP tests

The effect of slag replacement can be seen in relation to ϕ_{in} in Figs. 1–3 (a). On the one hand, an increase of slag from S20 to S40 led to a decrease of over 15% in ϕ_{in}, comparing both at 28 days. However, when the replacement is higher, which is the case of S60, almost no variations in ϕ_{in} were found with respect to S20 at 28 days. Since C-S-H formation by slag occurs later in time, there is a lower C-S-H formation degree at 28 days due to the dilution of clinker as slag replacement increases. In this sense, the highest values of d_{th}(TG) and d_{th}(5%) obtained for S60 reveal a greater porosity when compared to those for S20 and S40 at 28 days. It has been found [1–3,35] that durability-related performance of

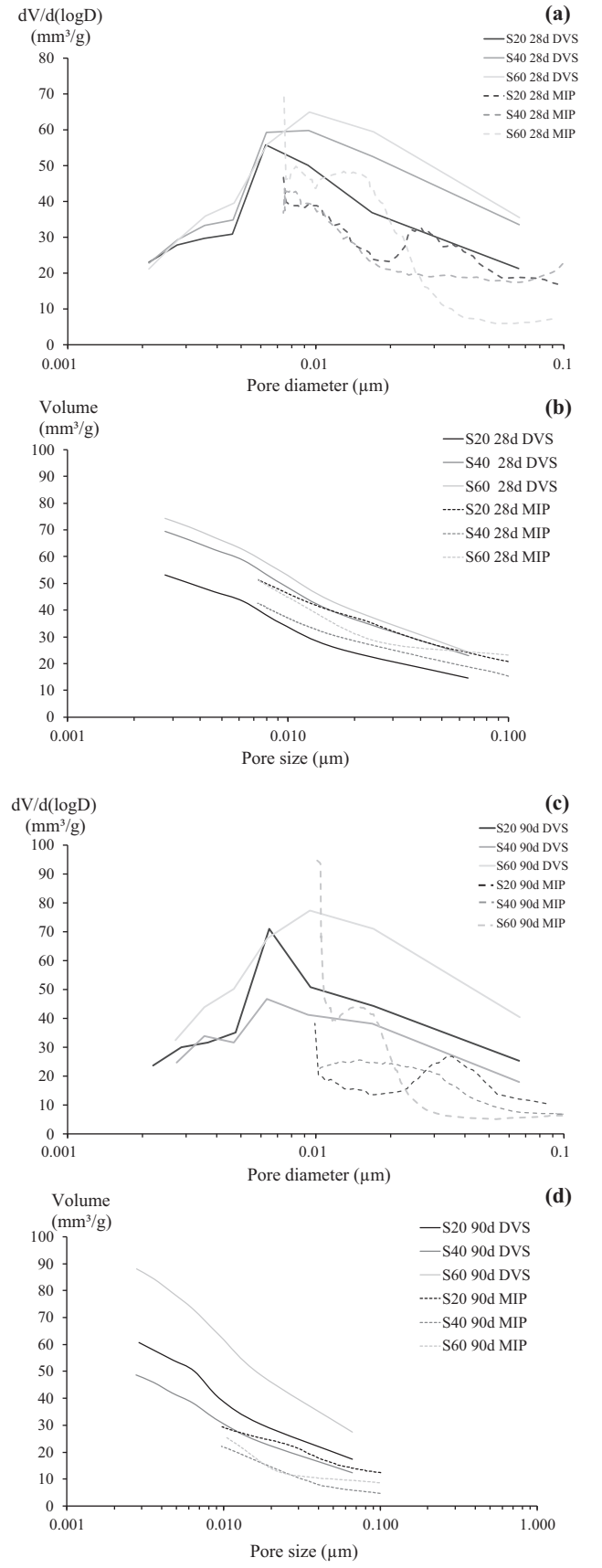

Fig. 6. Pore size distribution of S20, S40, and S60: derivative (a) and cumulative (b) at 28 days, and derivative (c) and cumulative (d) at 90 days, calculated with the BJH method on DVS data and MIP data.

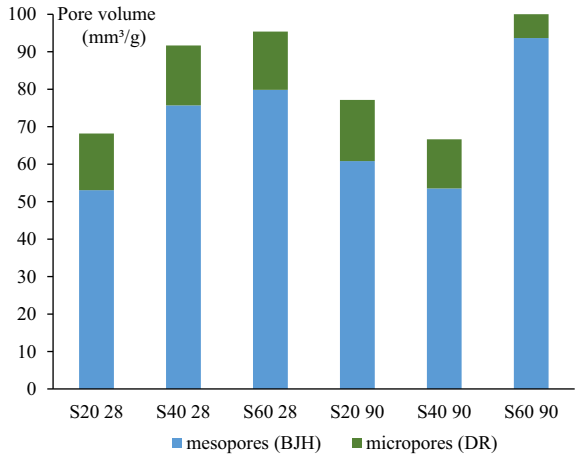

Fig. 7. Pore volume of mesopores and micropores using BJH and DR calculations respectively, for all mixes at 28 and 90 days, obtained from DVS data.

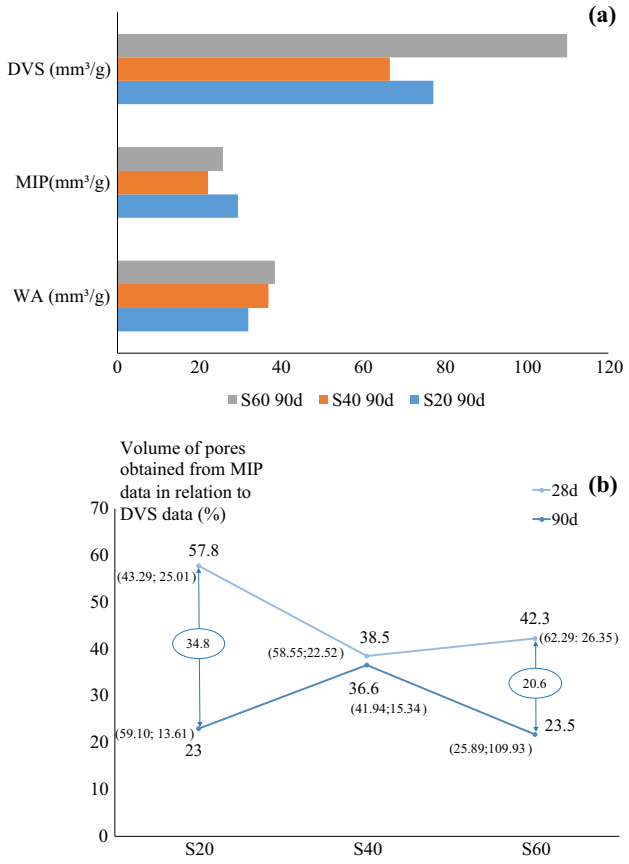

Fig. 8. Porosity obtained by WA, MIP and DVS: total pore volume (a); mesopore (b) volume from MIP data relative to mesopore volume from DVS data.

concrete with slag replacement up to 50% is superior in comparison to higher levels of replacement. Thus, it is expected that S40 and S20 have a lower porosity than S60. In relation to d_{min}, there were no significant variations in any of the mixtures at 28 days. This parameter is only related to the maximum pressure achieved and therefore does not provide very useful information.

Microstructural changes over time are seen when comparing Figs. 1–3 (a) to 1–3 (b). These figures show a clear reduction of more than 50% in ϕ_{in} when comparing results at 28 and 90 days for all mixes. Accordingly, there is also a reduction in the values of the d_{th} at 90 days, in all mixes, when calculated with the tangent method and in all but S20 (which remained practically the same) when calculating with the 5% method. This reduction of the accessible porosity is related to the filling of capillary pores with hydration products from the slag, which narrows down the pore structure. Several authors [3,36–38] have also found refinement of pores with time when replacing certain percentages of cement with slag.

The shape of the cumulative curves also provides information regarding the pore structure. Especially in the case of S60, a strong presence of "choke points" can be seen in the range between 0.03 and 0.2 μm. The flatness of the curve followed by a steep rise indicates that a relatively high increase in pressure had to be applied until a certain pore size could be filled. After these pressure increases, some large pores with narrow throats may be filled (but accounted for as smaller pores since increasing pressures are needed to fill smaller and smaller pores). This has been highlighted by Diamond [21], who stated that most of the pores can only be reached by mercury through a long percolative chain of intermediate pores of varying sizes and shapes. Here, the main discrepancy with the theoretical assumptions is brought to light, given that the presence of this kind of constrictions in the pore network is expected because of the specific nature of cementitious materials instead of the idealised cylinder-shape pores.

As pressure increases, there is no uniform ingress depth of mercury, since it depends on the amount of the restrictive pore sizes. This effect is described as lost porosity, and Alford and Rahman [39] suggested that only part of this lost porosity should be attributed to the fine end of the pore size distribution, accounting the rest to large pores that are enclosed by pores that are too narrow to be intruded by MIP. The s-shaped curve mainly represents this lack of uniformity in the mercury penetration rate, due to the pressure increase governed by the presence of certain restrictive pore sizes. It has been found in mortars with silica fume and mortars with slag [40] that the sharp threshold seen for the cement paste is lost when sand is used. In fact two threshold diameters can be identified when silica fume and slag is used. But this does not occur for the mortars without slag or silica fume. The authors do not mention this difference, but it is likely that this difference in the shape of the cumulative curve is given by the presence of restrictive pore sizes due to the use of SCMs.

Taking this into account, calculations of the primary and secondary threshold diameters were made, especially for S20 and S60 a strong presence of choke points can be seen in the cumulative curves. Values of d_{th2}(TG) are always higher than d_{th1}(TG), but since the steps in the cumulative curve are not representative of the actual pore size distribution, the value of d_{th2}(TG) is a virtual parameter and cannot account for an actual pore size. Then, the slope of the first segment of the curve before the first inflection point is more reliable, in relation to the pore size, than the following part of the curve. However, d_{th2}(TG) provided information regarding the presence of choke points. The difference between the intruded pore volume between the last point of the fitting line used for d_{th1}(TG) and the first point of the fitting line used for d_{th2}(TG) was calculated for S20, S40 and S60. The result is the volume of mercury intruded into the restrictive pores, indicated in the flatness of the curves. This value was designated as "virtual tortuosity volume"(VTV), and portrays the volume of restrictive or "choke points". After the slope changes suddenly, a high amount of mercury rapidly ingresses into pores which are not actually equivalent to the pore size that the pressure level represents in accordance with the Washburn equation. Values of VTV obtained at 28 and 90 days were: 19.36 mm^3/g and 11.96 mm^3/g for S20, 6.67 mm^3/g and 7.83 mm^3/g for S40, and 20.56 mm^3/g and 13.27 mm^3/g for S60. For S40, since there is not a clear presence of choke points according to the shape of the MIP curve, there is

also little change with time. The influence of slag with time can be seen especially for S20 and S60 mixes, since there is a clear reduction in the volume of the VTV for both cases. The decrease of choke points as a function of age is generally attributed to C-S-H gel formation, and autogenous shrinkage [23]. This indicates that the pore connectivity and the presence of restrictive pore sizes have more influence than the pore volume on the accessibility into the matrix. For example, the high amount of intruded mercury in the smallest pores range for S60, shown in Fig. 3 (a), cannot be directly used to compute the equivalent volume of this pore size range. As explained before, some restrictive pore sizes, choke points represented by the VTV, are most likely responsible for the pressure rise until larger pores are reached.

Considering the aforementioned results from MIP data, both primary and secondary values of d_{th} obtained with the tangent method and ϕ_{in} were found to be the most representative parameters.

4.2. DVS tests

From DVS results shown in Fig. 5 (a) and (b), an abrupt decrease can be seen in the desorption curve below 40% RH. This can be explained by constriction effects of the microstructure [20], on the basis of a similar hypothesis to that used for MIP data. In this sense, Snoeck et al. [14] suggested that mainly ink bottle pores may be responsible for this steep decrease. They explained that if the diameter of the pore entrance is smaller than a certain critical width, the mechanism of desorption from the pore body involves the spontaneous nucleation and growth of gas bubbles in the metastable condensed fluid. In this case, the body empties while the pore neck remains filled. In the case of the sorption curve, the steep rise above 60% RH shows the menisci formation in the pores. This leads to the marked hysteresis that all the curves have. The different path between the desorption and the sorption curve has been described in many cases for porous materials [8,14,15,41–44]. The network theory explains this hysterical behaviour considering the existence of controlling pore size entries that govern the dynamics of water ingress [44]. In that sense, the net pore volume also has less influence than the pore connectivity and the presence of restrictive pore sizes on the accessibility into the matrix. The different paths inside the microstructure define to what extent the water inside the pores vaporizes or condensates according to the amount of connectivity they have.

The calculations for the pore volumes, using the BJH method (Fig. 7), show an increase in the mesopore range at 28 days as the slag replacement increases. The increase is particularly noticeable when comparing S20 to S40, and can be seen in the rise of the slope of the sorption curve when RH is higher than 80%. This is in agreement with findings from Snoeck [45], who also found a higher amount of mesopores as slag replacement increased when performing DVS tests on pastes with 15%, 50%, and 85% of slag. Fig. 6 also shows the pore size distribution obtained from MIP data, where a difference in shape is noticeable for the curve obtained with the BJH method. The delayed intrusion into the smallest pores for the case of MIP leads to a virtual pore size distribution of the smallest range of the pore size distribution. From these graphs, the irregular distribution of pore size for MIP results can also be considered evidence of the presence of choke points, in comparison with the distribution curves for DVS, which are more continuous and less sensitive to ink-bottle shapes.

The values of resistivity in the saturated state (see Table 1) also reflect the combined effect of increase in tortuosity and the eventual decrease in the pore solution conductivity with increasing slag content. When comparing these results with the accessible porosity calculated from WA, the increase in pore volume (and hence water volume in the saturated state) is not followed by a reduction in resistivity; changes in pore connectivity, tortuosity and the decrease in the ionic strength are thus considered responsible for this effect of the increasing inclusion of slag. However, the quantification of the relative contributions from the physical and chemical effects require complementary analyses of the pore liquid. Future studies are planned to further investigate this relationship in slag blended cementitious materials.

When comparing the results of the mixes at 90 days, S20 and S60 relatively have the same hygroscopic behaviour, however, this does not mean that the microstructure has not been affected by the presence of the slag. Results of the calculations made with the BJH and DR methods, shown in Fig. 7, indicate that both S20 and S60 have more volume of mesopores at 90 days than at 28 days. It could be possible that a certain volume of macropores (out of the range of mesopores that BJH is intended for) turned into mesopores sometime between 28 and 90 days, because of the pore refinement effect over time caused by the presence of slag. Generally, slag affects tortuosity and refines pores, but does not significantly diminish pore volume [2,3,36–38,46]. Therefore, it is possible that the increase in the volume of mesopores at 90 days for S20 and S60 can be caused by the shift of certain volume of macropores into mesopores.

Particularly in the case of S20, comparing the results at 28 and 90 days, the major difference in the volume amount is at the peak shown in the range of 0.006–0.007 μm. Therefore, the volume increase is concentrated in the increase in the narrow mesopore range.

For the case of S40, at 90 days there is a significant reduction in the pore volume. This is seen in the reduction of the water uptake, represented by the slope of the isotherm curve at 90 days. Moreover, calculations of the pore size distribution with the BJH and DR methods shown in Fig. 7 reveals reductions in the mesopore range as well as in the micropore range. It seems that the mix with 40% replacement has the best performance regarding the development of pore structure. Considering that porosity and strength are intimately related, similar conclusions have been drawn by [46], who found that 40% cement replacement with GGBFS yields the hydration products caused by latent hydraulic activity which fill the pores, resulting in the mix with the overall best performance when compared to mixes S20 and S60.

Finally, results of the pore size distribution and total pore volume (intrudable/accessible to water molecules) obtained from the DVS tests differ from those obtained from the MIP tests, but can be complementary at the same time. The differences are expected since they measure different pore size ranges and they have different approaches. Fig. 8 shows a proof of this, by displaying the ratio between the volume of mesopores assessed by the MIP test and by the DVS test. Only the mesopore range was chosen since the sum of micropores obtained with the DR formula and the mesopores obtained with the BJH method cannot account for the same value as ϕ_{in} obtained with the MIP test. In fact, pore size distributions obtained from MIP tests extend from 0.007 μm to 100 μm, and overlap with BJH pore size distributions, but do not reach the micropore range calculated from the DVS results with the DR methods (this can be seen in Fig. 6). In this sense, it is also likely that as MIP builds up high pressures, it causes a collapse of some of the finer pores, although this was minimized by limiting the pressure in the test set up.

It is interesting to notice that the ratio diminishes with time for S20 and S60, but not for S40. This means that the difference between the MIP results and the DVS results is bigger at 90 days than at 28 days, for S20 and S60. It seems that MIP is more sensitive to pore refinement with time. Furthermore, with age, the matrix becomes more stiff, leading to a higher resistance to pore collapse.

The reachable volume registered through DVS should be higher than MIP measurements, explaining the smaller values of porosity

obtained when using MIP compared to DVS. This difference has also been found by [42] and accounted for the differing abilities of these methods to sample different pore sizes. It should also be mentioned that total pore volume obtained by BJH on DVS data does not linearly correspond to total pore volume from MIP data. For example, S60 at 90 days has the highest value for pore volume from DVS data, but one of the lowest from MIP data. As mentioned before, this is attributed to the fact that MIP test provides virtual pore size distributions, especially in the smallest pore size ranges when ink-bottle and restrictive path effects have more influence. In this regard, Moro and Bôhni [47] suggested that the distribution curve obtained from MIP data should be called "pore throat" size distribution. Using image analysis to examine the pore size distribution and compare it with MIP results, Abell et al. [48] confirmed that the ink bottle effect increases the volume of smaller pores due to the presence of larger pores behind the bottle necks.

5. Conclusions

DVS and MIP analyses proved to be sensitive to the pore size distribution changes when testing mixes with different replacement amounts of OPC with GGBFS at 28 and 90 days.

From the DVS data, hysteresis can be seen in all mixes and at both ages. This is mainly attributed to the geometrical characteristics of the pores, especially enhanced in the gap between 40% RH and 60% RH. When comparing pore size distribution over time, S40 had the best evolution showing a significant volume decrease in the mesopore range. From MIP data, $d_{th}(TG)$ and ϕ_{in} were found to be the most representative parameters. In this sense, S40 had the highest reduction of d_{th} and over 50% reduction of ϕ_{in} at 90 days.

Differences in the values obtained with DVS and MIP are attributed to the actual differences in the measurements that both methods perform and in range of the pore sizes they describe. Results from both techniques are influenced to a different extent by the presence of restrictive pore sizes that limit the accessibility into other pores, leading to the conclusion that pore connectivity and pore size distribution have more influence on the results of both tests than total pore volume. In this sense, a shift of pore size distribution towards smaller sizes can be expected for MIP results, especially in the smallest pore size ranges where ink bottle and restrictive path effects may cause a delay in the intruded pore volume. However, this might also be the reason why MIP seems to be more sensitive to pore refinement with time than DVS. Results from DVS are also influenced by the presence of ink bottle pores, reflected by the hysteresis. The effect on the obtained pore size distribution is however lower than in the case of MIP, and with this technique it is still possible to reliably quantify the smallest pore sizes (up to 0.002 μm).

Considering the points discussed above it is difficult to have a preference for one technique or the other. Both MIP and DVS provided information regarding the pore size distribution and connectivity, and, simultaneously, they both proved to be sensitive to changes in the pore system with time. The results of both methods can be considered complementary to each other, providing information over a wide range of pore sizes.

Acknowledgements

As a Research Fellow of the Research Foundation-Flanders (FWO-Vlaanderen), D. Snoeck wants to thank the foundation for the financial support.

References

[1] Report of ACI Committee 233, Slag cement in concrete and mortar. ACI 233R-03, American Concrete Institute, Farmington Hills, Mich, 2003.
[2] J. Bijen, Benefits of slag and fly ash, Constr. Build. Mater. 10 (5) (1996) 309–314.
[3] A. Bouikni, R. Swamy, A. Bali, Durability properties of concrete containing 50% and 65% slag, Constr. Build. Mater. 23 (2009) 2836–2845.
[4] S. Kumar, R. Kumar, A. Bandopadhyay, T. Alex, B. Kumar, S. Das, S. Mehrotra, Mechanical activation of granulated blast furnace slag and its effect on the properties and structure of Portland slag cement, Cement Concr. Compos. 30 (2008) 679–685.
[5] P. Aïtcin, Binders for Durable and Sustainable Concrete, Taylor & Francis, 2008.
[6] E. Özbay, M. Erdemir, H. Durmus, Utilization and efficiency of ground granulated blast furnace slagon concrete properties – a review, Constr. Build. Mater. 105 (2016) 423–434.
[7] K.Y. Yeau, E.K. Kim, An experimental study on corrosion resistance of concrete with ground granulate blast-furnace slag, Cem. Concr. Res. 35 (2005) 1391–1399.
[8] V. Baroghel-Bouny, Water vapor sorption experiments on hardened cementitious materials. Part I: essential tool for analysis of hygral behavior and its relation to pore structure, Cem. Concr. Res. 37 (2007) 414–437.
[9] S. Bahador, H.C. Jong, Study on moisture transport and pore structure of pc and blended cement concrete by monitoring the weight loss during the drying process, in: 32nd Conference on our world in concrete & structures: 28–29 August 2007, 2007. Singapore. Article Online Id: 10003201.
[10] N. De Belie, J. Kratky, S. Van Vlierberghe, Influence of pozzolans and slag on the microstructure of partially carbonated cement paste by means of water vapour and nitrogen sorption experiments and BET calculations, Cem. Concr. Res. 40 (2010) 1723–1733.
[11] X. Chen, S. Wu, J. Zhou, Experimental study and analytical model for pore structure of hydrated cement paste, Appl. Clay Sci. 101 (2014) 159–167.
[12] M. Wu, B. Johannesson, M. Geiker, Application of water sorption measurements for porosity characterization of hardened cement pastes, Constr. Build. Mater. 66 (2014) 621–633.
[13] Q. Zeng, D. Zhang, H. Sun, K. Li, Characterizing pore structure of cement blend pastes using water vapor sorption analysis, Mater. Charact. 95 (2014) 72–84.
[14] D. Snoeck, L.F. Velasco, A. Mignon, Van. Vlierberghe, P. Dubruel, P. Lodewyckx, N. De Belie, The influence of different drying techniques on the water sorption properties of cement-based materials, Cem. Concr. Res. 64 (2014) 54–62.
[15] D. Dollimore, P. Spooner, A. Turner, The BET method of analysis of gas adsorption data and its relevance to the calculation of surface areas, Surf. Technol. 4 (1976) 121–160.
[16] E. Barret, L. Joyner, P. Halenda, The determination of pore volume and area distributions in porous substances – computations from nitrogen isotherms, J. Am. Chem. Soc. 73 (1951) 373–380.
[17] D.N. Winslow, M.D. Cohen, D.P. Bentz, K.A. Snyder, E.J. Garboczi, Percolation and pore structure in mortars and concrete, Cem. Concr. Res. 24 (1994) 25–37.
[18] R. Cook, K. Hoover, Mercury porosimetry of hardened cement pastes, Cem. Concr. Res. 29 (1999) 933–943.
[19] C. Leech, D. Lockington, R.D. Hooton, Estimation of water retention curve from mercury intrusion porosimetry and van Genuchten model, ACI Struct. J. 103 (2) (2006) 291–295.
[20] D. Panesar, J. Francis, Influence of limestone and slag on the pore structure of cement paste based on mercury intrusion porosimetry and water vapour sorption measurements, Constr. Build. Mater. 52 (2014) 52–58.
[21] S. Diamond, Mercury porosimetry: an inappropriate method for the measurement of pore size distributions in cement-based materials, Cem. Concr. Res. 30 (2000) 1517–1525.
[22] H. Ma, Mercury intrusion porosimetry in concrete technology: tips in measurement, pore structure parameter acquisition and application, J. Porous. Mater. 21 (2014) 207–215.
[23] K. Aligizaki, Pore Structure of Cement-Based Materials: Testing, Interpretation and Requirements, Taylor and Francis, 2006.
[24] P. Pipilikaki, M. Beazi-Katsioti, The assessment of porosity and pore size distribution of limestone Portland cement pastes, Constr. Build. Mater. 23 (2009) 1966–1970.
[25] Z. Liu, D. Winslow, Sub-distributions of pore size: a new approach to correlate pore structure with permeability, Cem. Concr. Res. 25 (4) (1995) 769–778.
[26] BS EN 196-1, Methods of testing cement. Determination of strength, 2005. ISBN: 0 580 45670 6.
[27] C. Ferraris, V. Hackley, A. Avilés, Measurement of Particle Size Distribution in Portland Cement Powder: Analysis of ASTM Round Robin Studies, Cement, Concrete and Aggregates 26 (2) (2004) 1–11, http://dx.doi.org/10.1520/CCA11920.
[28] M. Cyr, A. Tagnit-Hamou, Particle size distribution of fine powders by LASER diffractionspectrometry. Case of cementitious materials, Mater. Struct. 34 (2001) 342–350.
[29] V. Ramachandran, J. Beaudoin, Handbook of Analytical Techniques in Concrete Science and Technology, principles techniques and applications, in: J. Beaudoin, J. Marchand (Eds.), Chapter 14: Pore Structure, 1999, pp. 528–628.
[30] E.W. Washburn, The dynamics of capillary flow, Phys. Rev. 17 (1921) 273–283.
[31] J. Zhang, G.W. Scherer, Comparison of methods for arresting hydration of cement, Cem. Concr. Res. 41 (2011) 1024–1036.

[32] IUPAC, Manual of symbols and terminology. Appendix 2. Pt. 1. Colloid and surface chemistry, Pure Appl. Chem. (1972).
[33] M. Dubinin, Physical adsorption of gases and vapors in micropores, Prog. Surf. Membr. Sci. 9 (1975) 1–70.
[34] S. Brunauer, L. Deming, W. Deming, Teller, J. Am. Chem. Soc. 62 (1940).
[35] G.J. Osborne, Durability of Portland blast-furnace slag cement concrete, Cement Concr. Compos. 21 (1999) 11–21.
[36] Ô. Cakır, F. Akoz, Effect of curing conditions on the mortars with and without GGBFS, Constr. Build. Mater. 22 (2008) 308–314.
[37] E. Aprianti, P. Shafigh, R. Zawawi, Fitri Abu Hassan Zahiruddin, Introducing an effective curing method for mortar containing high volume cementitious materials, Constr. Build. Mater. 107 (2016) 365–377.
[38] E. Gruyaert, P. Van den Heede, M. Maes, N. De Belie, A comparative study of the durability of ordinary portland cement concrete and concrete containing (high) percentages of blast-furnace slag, in: International RILEM Conference on Materials Science – MATSCI, Aachen 2010 – Vol. III, 2010. AdIPoC.
[39] N. Alford, A.A. Rahman, An assessment of porosity and pore sizes in hardened cement pastes, J. Mater. Sci. 16 (11) (1981) 3105–3114.
[40] D. Winslow, M. Cohen, Percolation and pore structure in mortars and concrete, Cem. Concr. Res. 24 (1994) 25–37.
[41] K. Sing, Adsorption methods for the characterization of porous materials, Adv. Colloid Interface Sci. 76–77 (1998) 3–11.
[42] P. Monson, Understanding adsorption/desorption hysteresis for fluids in mesoporous materials using simple molecular models and classical density functional theory, Microporous Mesoporous Mater. 160 (2012) 47–66.
[43] A. Kumar, S. Ketel, K. Vance, T. Oey, N. Neithalath, G. Sant, Water vapour sorption in cementitious materials – Measurement, modeling and interpretation, Transp. Porous Media 103 (2014) 69–98.
[44] Zaccardi Y. Villagrán, A. Di Maio, R. Romagnoli, The effect of slag and limestone filler on resistivity, sorptivity, and permeability of concrete with low paste content, Mater. Res. Soc. Symp. Proc. 1488 (2012).
[45] D. Snoeck, Self-Healing and Microstructure of Cementitious Materials with Microfibres and Superabsorbent Polymers, Ghent University, Ghent, 2015.
[46] M. Shariq, J. Prasad, A. Masood, Effect of GGBFS on time dependent compressive strength of concrete, Constr. Build. Mater. 24 (2010) 1469–1478.
[47] F. Moro, H. Bôni, Ink-bottle effect in mercury intrusion porosimetry of cement-based materials, J. Colloid Interface Sci. 246 (2002) 135–149.
[48] A. Abell, K. Willis, D. Lange, Mercury intrusion porosimetry and image analysis of cement-based materials, J. Colloid Interface Sci. 211 (1999) 39–44.